# Monitoring the optical turbulence in the surface layer at Dome C, Antarctica, with sonic anemometers

E. Aristidi, J. Vernin, E. Fossat, Schmider F.X., T. Travouillon, C. Pouzenc, O. Traullé, C. C. Genthon, A. Agabi, E. Bondoux, et al.

Monthly Notices
of the
ROYAL ASTRONOMICAL SOCIETY

MNRAS **454,** 4304–4315 (2015) doi:10.1093/mnras/stv2273

# Monitoring the optical turbulence in the surface layer at Dome C, Antarctica, with sonic anemometers

E. Aristidi,[1]⋆ J. Vernin,[1] E. Fossat,[1] F.-X. Schmider,[1] T. Travouillon,[2] C. Pouzenc,[3] O. Traullé,[4] C. Genthon,[5] A. Agabi,[1] E. Bondoux,[1] Z. Challita,[6] D. Mékarnia,[1] F. Jeanneaux[1] and G. Bouchez[7]

[1]*Laboratoire Lagrange, Université Côte d'Azur, Observatoire de la Côte d'Azur, CNRS, Parc Valrose, F-06108 Nice Cedex 2, France*
[2]*Thirty Metre Telescope, 1111 South Arroyo Parkway, Pasadena, CA 91105, USA*
[3]*Observatoire Sirene, F-84400 Lagarde d'Apt, France*
[4]*CNRM-GAME, URA F-1357, Météo France CNRS, Toulouse, France*
[5]*LGGE, UJF-CNRS, 54, rue Molière BP 96, F-38402 Saint-Martin, d'Hères cedex, France*
[6]*Aix Marseille Université, CNRS, LAM (Laboratoire d'Astrophysique de Marseille) UMR 7326, F-13388, Marseille, France*
[7]*GEMAC, University of Versailles/CNRS, 45 av. des Etats-Unis, F-78035, Versailles Cedex, France*

Accepted 2015 September 29. Received 2015 September 8; in original form 2015 July 15

**ABSTRACT**

The optical turbulence above Dome C in winter is mainly concentrated in the first tens of metres above the ground. Properties of this so-called surface layer (SL) were investigated during the period 2007–2012 by a set of sonic anemometers placed on a 45 m high tower. We present the results of this long-term monitoring of the refractive index structure constant $C_n^2$ within the SL, and confirm its thickness of 35 m. We give statistics of the contribution of the SL to the seeing and coherence time. We also investigate properties of large-scale structure functions of the temperature and show evidence of a second inertial zone at kilometric spatial scales.

**Key words:** turbulence – atmospheric effects – methods: data analysis – site testing.

## 1 INTRODUCTION

During the last two decades, the Antarctic Plateau has been attracting interest from the astronomical community. Since the first site-testing experiments at the South Pole (Marks et al. 1999), a lot of work has been done, especially after the advent of the French–Italian station Concordia at the summit of Dome C. This work revealed very interesting qualities for astronomy. Its altitude (3300 m) combined with low humidity is expected to give excellent transparency and low sky background emissivity in the infrared (Lawrence 2004). The good meteorological conditions combined with its location near the Pole (75°S) give access to high temporal coverage (Mosser & Aristidi 2007). In winter the seeing was found to be excellent (about 0.4 arcsec) above a thin surface layer (SL) of thickness close to 30 m (Lawrence et al. 2004; Trinquet et al. 2008; Aristidi et al. 2009). Seeing stability studied by Fossat et al. (2010) reported periods of 7–8 h where the seeing was continuously below 0.5 arcsec.

Other polar stations were investigated in Antarctica: Dome A (Bonner et al. 2010) and Dome F (Okita et al. 2013). Similar properties were found at these locations, in particular this thin SL which gives access to the free atmosphere seeing at elevations of a few tens of metres above the ground. This is also supported by numerical simulations by Swain & Gallée (2006), Hagelin et al. (2008), Lascaux et al. (2009), Lascaux, Masciadri & Hagelin (2010) and Lascaux, Masciadri & Hagelin (2011). Therefore, the characterization of the SL, in terms of both intensity and vertical structure, is critical to the determination of methods to compensate its effects (Travouillon et al. 2009; Carbillet et al. 2010). So far, our knowledge of the SL comes from several instruments, but each one has specific flaws. Early SOnic Detection And Ranging (SODAR) measurements, for example, did not have the vertical resolution to resolve the SL turbulence (Lawrence et al. 2004). Balloon-borne microthermal sondes do have the vertical resolution but lack the temporal resolution necessary to obtain a statistically meaningful data set (Trinquet et al. 2008). Recent SODAR monitoring do have temporal and spatial resolution, but do not provide a reliable estimate of the turbulence intensity (Petenko et al. 2014).

In situ measurements therefore became a viable option. The presence of a 45 m tower (Fig. 1) allowed the possibility of these measurements. First attempts were made during the first winter-over in 2005, with microthermal sensors (Azouit & Vernin 2005) at different locations on the tower. However, they appeared to be too fragile in the windy and icy conditions and no reliable results could be obtained. An alternative to microthermal sensors which uses similar principles to measure optical turbulence without the issue of brittleness is sonic anemometers. Their use in the study of atmospheric turbulence was discussed by Kaimal (1979) and more recently by

⋆E-mail: aristidi@unice.fr

**Figure 1.** The 45 m tower at Dome C. Computers and electronic equipments are located in the shelter at the foot of the tower.

Travouillon et al. (2015). Their principle is to make a high speed measurement of temperature and wind velocity vector, which are processed to obtain an estimate of the optical turbulence structure constant $C_n^2$. Using several sonic anemometers along the height of the tower allows us to make discrete measurements of the turbulence profiles only limited in vertical resolution by the number of instruments used. Our instrumentation and the first result were introduced in Travouillon et al. (2008, 2010). The scope of this paper is to present our data processing method based upon temperature structure functions, and local turbulence measurements in terms of refractive index structure constant $C_n^2$ obtained between 2007 and 2012.

The paper is organized as follows. Section 2 recalls theoretical concepts about the optical turbulence. The experimental setup is described in Section 3. Data processing, error analysis, sources of biases and instrument calibration are presented in Section 4. Results are shown in Section 5.

## 2 THEORY

Turbulence discussed in this article is the optical turbulence, which is related to spatial and temporal heterogeneities of the refractive index. These heterogeneities result from both the meteorological turbulence (vortices themselves) and gradients of the temperature and the wind speed (in particular the vertical temperature gradient). At Dome C, during the polar winter, strong temperature inversions are observed in the first tens of metres above the snow surface (Trinquet et al. 2008; Genthon et al. 2013). This is a very stable situation and meteorological turbulence is mostly inhibited in this case. But the few meteorological turbulence that remains induces strong optical turbulence because of these strong temperature gradients.

Atmospheric optical turbulence is often described by a set of quantities such as the seeing $\epsilon$, the isoplanatic angle $\theta_0$, the coherence time $\tau_0$ or the spatial coherence outer scale $\mathcal{L}_0$. These parameters all result from an integration along the line of sight of local quantities such as the wind speed and the structure constant of the refractive index $C_n^2$. Theoretical basis of the effects of optical turbulence in astronomy is described in the review paper of Roddier (1981), and we will here pick up some particular points of interest for the present study.

Turbulent air flows are characterized by random wind speed and temperature fluctuations. The temperature structure function is among the statistical quantities describing the temperature fluctuations at two points separated by a distance $\rho$ and is given by

$$D_{\mathrm{T}}(\boldsymbol{\rho}) = \langle (T(\boldsymbol{r}) - T(\boldsymbol{r}+\boldsymbol{\rho}))^2 \rangle \tag{1}$$

where $r$ is the position of one point, $T$ the temperature and $\langle\rangle$ stands for ensemble average. This function behaves as a power law in $\rho^{\frac{2}{3}}$ when $\rho = |\boldsymbol{\rho}|$ is between the dynamic inner scale $l_0$ and the outer scale $L_0$. These scales can be seen as the sizes of the smallest and largest eddies of the turbulent air flow. Outside the interval $[l_0, L_0]$ (so-called inertial range) the structure function tends towards a constant. Within the inertial range, one defines the structure constant of the temperature $C_{\mathrm{T}}^2$ as

$$D_{\mathrm{T}}(\boldsymbol{\rho}) = C_{\mathrm{T}}^2 \rho^{\frac{2}{3}} \tag{2}$$

and making use of Gladstone's law which links the refraction index to the temperature, the structure constant of the refractive index $C_n^2$ expresses as

$$C_n^2 = 6.24 \times 10^{-9}\, C_{\mathrm{T}}^2\, P^2\, T^{-4} \tag{3}$$

with $T$ in kelvin and the pressure $P$ in hPa. The seeing as seen by a telescope at an elevation $h_0$ is computed by the following integral over the altitude $z$ ($\epsilon$ is here in radian and $\lambda$ is the wavelength):

$$\epsilon = 5.25\, \lambda^{-1/5} \left[ \int_{h_0}^{\infty} C_n^2(z)\, \mathrm{d}z \right]^{\frac{3}{5}}. \tag{4}$$

The coherence time is deduced from both the $C_n^2$ profile and the wind speed profile $|V(z)|$

$$\tau_0 = 0.058\, \lambda^{6/5} \left[ \int_{h_0}^{\infty} |V(z)|^{5/3}\, C_n^2(z)\, \mathrm{d}z \right]^{-\frac{3}{5}}. \tag{5}$$

## 3 THE SONIC ANEMOMETERS

The experiment is based upon a set of sonic anemometers installed on a tower located about 900 m West from the Concordia buildings. These anemometers are modified Sx probes from Applied Technologies Inc. They are composed of three pairs of ultrasonic transducers capable of measuring the wind speed in three orthogonal axes (namely $U$, $V$ and $W$, where $W$ is the vertical axis), as well as the temperature $T$. They are placed on horizontal bars pointing in the upwind direction to void the possibility of local effect due to the mast. Principle of the measurement involves the dependence of the transit time of acoustic pulses with the velocity of the wind. The time difference between two pulses travelling between

**Table 1.** Technical specifications of the sonic anemometers (from App. Tech. Inc).

| | |
|---|---|
| Temperature range | −80°C to +60°C |
| Wind speed range | 0 to 30 m s$^{-1}$ |
| Wind speed accuracy | 0.03 m s$^{-1}$ |
| Temperature accuracy | |
| Absolute | 2°C |
| Relative | 0.1°C |

a pair of transducers in opposite directions is indeed proportional to the wind speed, whereas the sum of these transit times gives the speed of sound, related to the temperature (see Friehe 1976 and references therein). The four numbers are provided at a rate of 10 Hz, a sampling high enough to infer the properties of turbulence, and in particular to estimate the structure constants $C_{\rm T}^2$ and $C_n^2$ as described in Section 4.1. Technical specifications of the anemometers are given in Table 1.

These instruments were modified in order to operate in the low temperatures of the Antarctic Plateau. The modification consists of a layer of aerogel which thermally insulates the sensing parts of the instruments, as well as a wrap of heating resistances that warms the units and protects them from ice formation. A cycle alternates between heating the probes and measuring (no measurement is possible during the heating since it would create unwanted local turbulence). After some trials we found that a 20 min period cycle with 10 min of heating and 10 min of measurements is a good compromise. The first few minutes (typically 2–3 min) after the heater has been turned off are contaminated by noise and are eliminated during the data processing. Still, in winter it is sometimes necessary to climb on the tower and manually remove the accumulated snow.

Three of these anemometers were installed in 2006 November (the tower was then 30 m high) at heights 8, 17 and 28 m above the snow surface. Because of sinking and snow accumulation, heights tend to decrease at a rate of $\simeq$10 cm yr$^{-1}$. These three sonics were operated during the whole first year, though the 17 m one suffered from a technical problem that reset its calibration parameters. The probe was recalibrated in 2008 January and the data could be corrected afterwards by software. The tower was extended by 15 m in 2007 December to attain a height close to 45 m, and three additional anemometers were installed on the new section. The heights of the sonics became 8 m, 17 m, 24 m, 31 m, 39 m and 45 m [the heights of the instruments were remeasured at the end of 2010 by Genthon et al. (2013) who found values a few per cent lower.]. This six-sonic setup was first operated in 2008 January. The 2008 data present some gaps due to various problems (crash of the computers, problems with heaters' power supplies). Then, in 2009 we obtained a very good set of data, though the 24 m probe stopped to work in March. It was replaced in 2009 November by the 45 m one, and the experiment ran with five sonics in 2010. Two other anemometers broke down at the beginning of 2011, as well as the entire heating system which could not be repaired in winter due to the harsh conditions. Three sonics could be repaired for the winter 2012, and the system worked well up to 2012 May.

The journal of the observations is summarized in Fig. 2, showing the number of data collected month by month by each sonic, after filtering of the bad points. It shows, unsurprisingly, that there are much more data in summer (ground temperature around −30°C) than in winter (temperature around −65°C). It also shows that the highest anemometer (45 m) collected less data than lower ones. Indeed, the temperature and the humidity of the air increase with the altitude (Genthon et al. 2013). The metallic structure of the upper part of the tower and of the highest anemometers are colder than the air surrounding and tend to ice up more frequently.

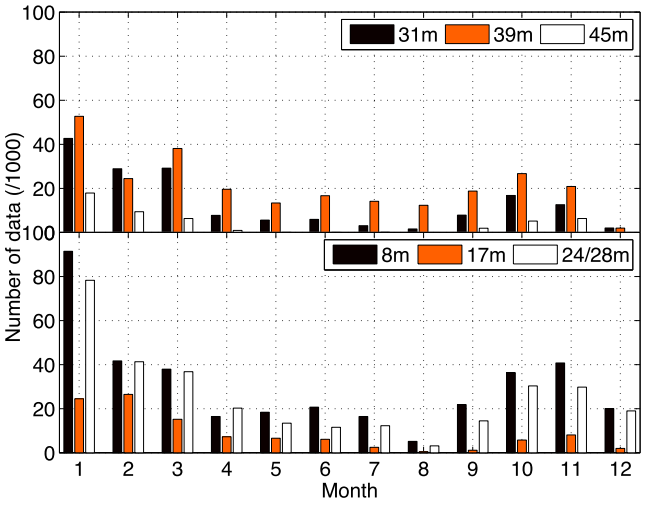


**Figure 2.** Number of data samples collected by each sonic every month from 2006 November to 2012 May. One data sample corresponds to 1 min of measurement. Top: the three upper sonics. Bottom: the three lower ones (the third was at height 28 m in 2006–2007, then at height 24 m).

## 4 DATA PROCESSING

### 4.1 $C_n^2$ measurements from sonic data

Sonic anemometers are connected to a data packer formatting the output of all the units so that they can be read directly from the RS232 port of a PC. One obtains an ascii file with four columns by sonic (containing the velocities $U$, $V$, $W$ and the temperature $T$) and one line every 0.1 s. That represents a volume of data of about 50 MB d$^{-1}$. A first preprocessing program scans these raw data in order to remove outliers.

Deriving the structure constant $C_n^2$ implies the estimation of the structure function $D_{\rm T}^2(\rho)$, i.e. to estimate the temperature fluctuations at two points separated by the distance $\rho$. As we have only one sensor at a given altitude, we use Taylor's hypothesis to transform $\rho$ in $\bar{v}\,\Delta t$ ($\bar{v}$ being the mean wind speed and $\Delta t$ a time interval between two measurements) and estimate the structure function as the temporal average

$$D_{\rm T}^2(v\,\Delta t) = \langle (T(t) - T(t+\Delta t))^2 \rangle. \quad (6)$$

Two methods were compared to compute the structure constant $C_{\rm T}^2$; they give similar results.

#### 4.1.1 *First method: structure function*

The aim is to estimate the full function $D_{\rm T}^2(\bar{v}\,\Delta t)$ by taking several values for $\Delta t$ (the sampling period is 0.1 s, so all the $\Delta t$ are multiples of 0.1 s). The temporal average has to be calculated on a time interval $\tau$ long enough to ensure statistical significance, but shorter than the characteristic time of evolution of $C_{\rm T}^2$. After some trials we found $\tau = 30$ min as a good compromise. Moreover, the wind speed modulus $\bar{v}$ which intervenes in $\bar{v}\,\Delta t$ was taken as a sliding average of $v = (U^2 + V^2 + W^2)^{1/2}$ over 1 s.

Fig. 3 shows an example of structure functions computed on data taken on 2007 June 12. The two curves correspond to the lowest (8 m) sonic, and the 28 m one. In log–log scale, both curves

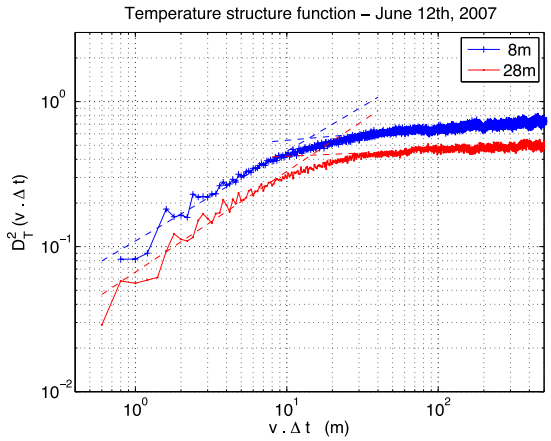


**Figure 3.** Structure functions computed from data taken on 2007 June 12. The upper curve corresponds to the 8 m sonic, and the lower one to the 28 m sonic. The dashed lines are least-squares fits of the inertial domain and on the saturation domain (large values of $\bar{v}\Delta t$).

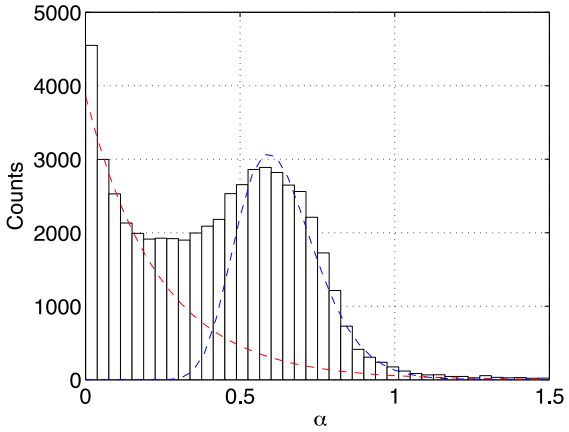


**Figure 4.** Histogram of the slopes $\alpha$ of the structure functions $D_T(\rho)$ of the sonic temperatures in the interval $\rho \in [0.6\text{ m}, 4\text{ m}]$. This histogram was computed from all six sonics data collected during the years 2008–2011. The dashed lines are (i) a negative exponential fit of the first part of the histogram for small values of $\alpha$, and (ii) a lognormal fit of the bump centred at $\alpha = 0.6$.

display a linear part in the interval [1 m, 10 m]. A least-squares fit of a function $C_T^2 \rho^\alpha$ (with $\rho = \bar{v}\ \Delta t$) was performed in this interval, and is displayed on the graph as a dashed line. It gave ($C_T^2 = 0.11 \pm 0.04\,\text{m}^{-2/3}$, $\alpha = 0.6 \pm 0.2$) for the 8 m sonic, and ($C_T^2 = 0.07 \pm 0.02\,\text{m}^{-2/3}$, $\alpha = 0.7 \pm 0.2$) for the 28 m sonic. The expected value of $\alpha$ being 2/3 in the inertial domain [$l_0$, $L_0$]. For large values of $\rho$ the structure function saturates as expected within the saturation region. Slopes were computed by least-squares fit in the saturation region, i.e. in the interval $\rho \in [100, 200]$ m. This interval was selected to make sure that it is well above the outer scale, and it has enough data points to reduce statistical noise. In the example of Fig. 3 we found slopes $\alpha = 0.09$ for the 8 m sonic and $\alpha = 0.04$ for the 28 m one. An estimation of the outer scale can be obtained at the intersection of the fits inside the inertial zone and inside the saturation region. We obtained $L_0 = 14$ m for the two heights.

Structure functions were computed on the whole set of data, and for each function a least-squares fit, as described in the example above, was performed on the interval $\rho \in [0.6\text{ m}, 4\text{ m}]$. This interval was selected after some trials, but its boundaries have little effect on the computed slopes and $C_T^2$: the change is 3 per cent on the slope and 2 per cent on $C_T^2$ if we use $\rho \in [1.2\text{ m}, 4\text{ m}]$; this is well below the error bars. Histogram of obtained slopes is shown in Fig. 4. It displays two features: a decreasing exponential-like curve for very small value of the slope $\alpha$, and a hump centred on the value $\alpha = 0.6$. This histogram mixes the data from all the anemometers, but individual ones look all the same, with even a more distinct separation between the two structures. Also there does not seem to be a dependence with the season (excepted that there are less data in winter so the histograms are more noisy). These two structures are characteristic of two different situations. The negative exponential is observed for very small slopes (its width is $\Delta\alpha = 0.15$) which indicates that corresponding data are in the saturation domain of the structure function and cannot be used to compute the parameter $C_T^2$. Indeed various types of data correspond to this case: frost or snow on the sensors (causing a random shape of the structure function), contamination by the heaters (the damping time after the heaters have been turned off is a few minutes), and other technical problems. These data will subsequently be removed from the analysis. The bump corresponds to slopes around $\alpha = 2/3$, with a dispersion $\Delta\alpha \simeq \pm 0.2$ (full width at half-maximum of the fitted lognormal curve is 0.4) of the same order of magnitude than the uncertainty given by the least-squares fit of the structure function. Data corresponding to this bump are in the inertial domain of the structure function and $C_T^2$ can be derived from them. They represent about 40 to 60 per cent of the data collected by each sonic.

### 4.1.2 *Second method: direct calculation*

This analysis presented in the previous section appears to be very efficient and provides a way of sorting the useful data, but the computation is very time consuming and one obtains only one value of $C_T^2$ every 30 min. An alternative is to compute one single point of the structure function for the smallest possible value of the time interval $\delta t = 0.1$ s, i.e. the quantity $[T(t) - T(t + \delta t)]^2$. The structure constant $C_T^2$ is estimated by the quantity

$$C_T^2 = \left\langle \frac{[T(t) - T(t + \delta t)]^2}{[v(t)\delta t]^{2/3}} \right\rangle_\tau \tag{7}$$

where the temporal average is made on a time $\tau = 1$ min. This method is a shortcut allowing quick computation of one value of $C_T^2$ every minute. Fig. 5 shows a comparison between $C_T^2$ computed both ways. The curve was obtained as follows: structure functions were computed every 30 min, giving a first set of $C_T^2$ values (we selected only data for which the slope of the structure function $\alpha > 0.4$. For the same 30 min periods, direct computation of 30 values of $C_T^2$ were calculated and averaged. The plot in Fig. 5 exhibits a strong linear relation between the two sets of $C_T^2$ with a slope of 1.02 and a correlation of 97 per cent. The two methods appear then to give consistent results. There is some scatter around the straight line of slope 1.02, of about 20 per cent, which is of the same order of magnitude than the statistical error on $C_T^2$ (see Section 4.4.1).

Finally, we adopted the following algorithm for deriving $C_n^2$ from sonic data:

(i) Split the data into 30 min intervals
(ii) Compute a structure function and check the slope $\alpha$.
(iii) If $\alpha < 0.4$ reject the 30 min interval
(iv) Otherwise compute 30 values of $C_T^2$ by the second method.

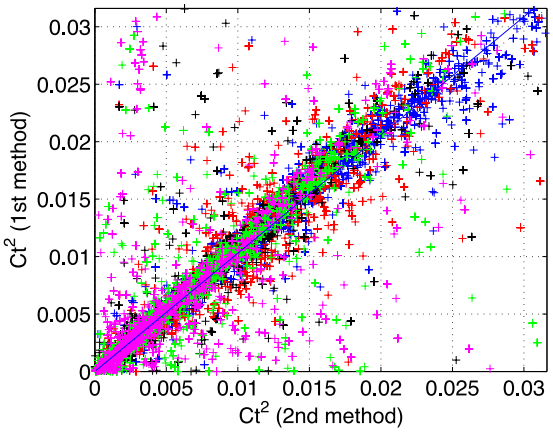


**Figure 5.** Comparison of $C_T^2$ values computed from the first method (fit of the inertial domain of the structure function) and the second method (direct computation from consecutive temperature values). Colours correspond to sonic elevation with the same convention as Fig. 10. The straight line is a least-squares fit of the data; its slope is 1.02.

(v) Calculate $C_n^2$ with equation (3), taking for $T$ the average temperature over 1 min, and for $P$ the mean yearly pressure of the site (645 hPa) since pressure fluctuations at Dome C are only a few per cent.

Hence, the structure functions were used only as a data filter, and the $C_T^2$ coefficients were computed via the direct method.

### 4.2 Dynamic outer scale $L_0$

As stated in Section 4.1.1, the computation of the structure function allows us to calculate the outer scale $L_0$ from a set of several tens of minutes of sonic data. Fig. 6 shows the graph of the median value of $L_0$ (computed from 1 h data samples) as a function of the height of the anemometer. The data were filtered so that the slope $\alpha$ of the log of the structure function in the inertial domain is greater than 0.4. Several thousands of reliable values for $L_0$ were obtained for each altitude.

The five first points of the graph appear to be almost aligned; a least-squares fit of a first-order polynom on these points, weighted by the inverse square of the error bars, shows a slope of 0.38 ± 0.04. It is indeed well known that the size $L$ of the eddies near the ground is $L = 0.4\,h$ where $h$ is the altitude (see e.g. Nakayama & Boucher 2000). Despite large error bars, this agreement gives us confidence in the validity of our outer scales and consolidates our data processing method.

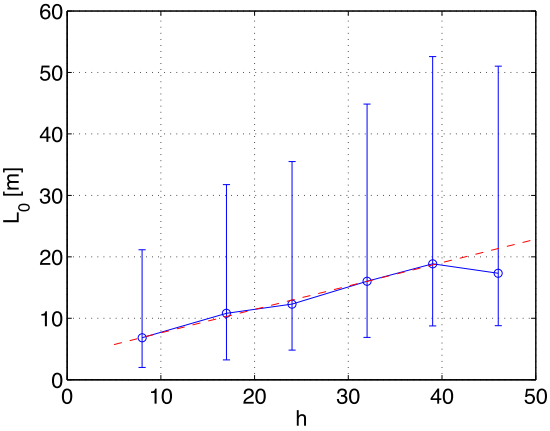


**Figure 6.** Outer scale $L_0$ as a function of the height of the anemometer. Error bars are the intervals containing 50 per cent of the data. The dashed line is a least-squares fit obtained on the five first points.

The last point of the graph, corresponding to the anemometer at height 45 m, is the less significative (2000 values instead of 4000 for the others).

### 4.3 Seeing and coherence time in the surface layer

The seeing is derived by integrating the structure constant profile $C_n^2(z)$ over the altitude $z$ (equation 4). The sonic data give access to the sonic seeing $\epsilon_s$ defined from equation (4) by replacing the upper limit of the integral by any value $h$ between $h_0$ and the height of the highest functioning sonic (ideally 45 m when the corresponding anemometer gives valid data). The wavelength $\lambda$ was set to 500 nm. This quantity $\epsilon_s$ is the contribution of the SL (between $h_0$ and $h$) to the seeing. Computation of the integral was performed assuming a second-order polynomial dependence of $\ln C_n^2(z)$ with the altitude. The three coefficients of the polynom were adjusted by least square on each set of simultaneous $C_n^2$ values. For situations where only two anemometers were functioning, we computed a first-order polynomial fit of $\ln C_n^2(z)$ instead of a second-order one.

Estimation of the sonic coherence time $\tau_s$ is very similar to the seeing, since the anemometers provide the wind speed and the constant $C_n^2$. As for the seeing, it is defined from equation (5) by replacing the upper limit of the integral by $h$. $\tau_s$ is the contribution of the atmospheric layer between $h_0$ and $h$ to the total coherence time $\tau_0$. The integral is computed the same way as the seeing.

### 4.4 Error analysis

#### *4.4.1 Error on $C_T^2$*

From equation (7) one can estimate the standard deviation $\sigma_C$ of the constant $C_T^2$ averaged over a 1 min data sample (which represents a number $n = 600$ values at the sampling period $\delta t = 0.1$ s). Assuming independence between consecutive sets of measurements we would have

$$\frac{\sigma_C}{C_T^2} = \frac{1}{\sqrt{n}}\left[4\frac{\sigma^2_{(\delta T)}}{(\delta T)^2} + \frac{4}{9}\frac{\sigma_v^2}{v^2}\right]^{1/2} \quad (8)$$

where $\sigma_v^2$ is the variance of $v$, $\delta T = [T(t) - T(t + \delta t)]$ and $\sigma^2_{(\delta T)}$ is its variance. However, at our sampling rate there remains some correlation between consecutive measurements. Indeed, the temporal autocorrelation function of the temperature shows a negative exponential decay at the origin, with a damping time of several tenths of seconds, sometimes 1 s. Taking 0.5 s for the correlation time of the temperature, the number $n$ of independent measurements in 1 min is $n = 120$. We will assume $n = 100$ in the following.

The lowest value of $\delta T$ is the precision of the temperature fluctuation measurement, i.e. $\delta T = 0.1$ K (Table 1). Its variance is $\sigma^2_{(\delta T)} = 2\sigma_T^2 - 2\,\mathrm{Cov}[T(r), T(r + \delta t)]$, $\sigma_T^2$ being the variance of the temperature, and $\mathrm{Cov}[T(r), T(r + \delta t)]$ the covariance between successive temperature measurements. A conservative value of $\sigma^2_{(\delta T)}$ is then $2\sigma_T^2$. Since the temperature is measured with an accuracy of 0.1 K, we have $\sigma^2_{(\delta T)} \simeq 0.02$ K$^2$ which was verified experimentally on the data. The first term of the sum in the above equation is then of the order of $4\frac{\sigma^2_{(\delta T)}}{(\delta T)^2} \simeq 8$.

The term $\sigma_v$ contains both the accuracy of the anemometers for wind speed measurement (0.03 m s$^{-1}$, see Table 1) and the

fluctuations of the wind speed during a 1 min time interval. It was estimated experimentally to $\sigma_v \simeq 0.5$ m s$^{-1}$. Taking a small value of $v = 1$ m s$^{-1}$, which is around the 10 per cent percentile of the wind speed distribution (Travouillon et al. 2008), the term $\frac{4}{9}\frac{\sigma_v^2}{v^2}$ is less than 0.1 and thus negligible in the above sum.

Finally, the relative error on the structure constant $C_T^2$ (assuming $n = 100$) is $\frac{\sigma_C}{C_T^2} \simeq 28$ per cent (it would have been 12 per cent with $n = 600$).

#### 4.4.2 Error on $C_n^2$

From equation (3) the error $\sigma_n$ on the refractive index structure constant can be expressed as

$$\frac{\sigma_n}{C_n^2} = \left[\left(\frac{\sigma_C}{C_T^2}\right)^2 + 4\left(\frac{\sigma_P}{P}\right)^2 + 16\left(\frac{\sigma_T}{T}\right)^2\right]^{1/2} \quad (9)$$

with $\frac{\sigma_P}{P}$, the relative error on the pressure, being of the order of 2 per cent and $\frac{\sigma_T}{T} \simeq 0.05$ per cent this error budget is largely dominated by the error on $C_T^2$. Therefore, the relative error on $C_n^2$ is also of the order of 28 per cent.

#### 4.4.3 Error on the seeing

The sonic seeing $\epsilon_s$ is defined by equation (10). A crude approximation of the integral is given by

$$S = \int_{h_0}^{h} C_n^2(z)\,\mathrm{d}z \simeq \sum_{i=1}^{5} C_{ni}^2 \Delta z_i \quad (10)$$

where $C_{ni}^2$ is the structure constant given by the sonic number $i$, and $\Delta z_i$ the distance between two consecutive sonics ($\Delta z_i \simeq 7$ m is almost the same for each sonic pair). The error $\sigma_S$ of this integral is deduced from the individual errors $\sigma_n^2$ of the $C_n^2$ of each sonic. We have, assuming negligible uncertainty for $\Delta z_i$,

$$\sigma_S = \left[\sum \sigma_{ni}^2 \Delta z_i^2\right]^{1/2} \simeq 0.28 \left[\sum C_{ni}^4 \Delta z_i^2\right]^{1/2}, \quad (11)$$

the factor of 0.28 above comes from the fact that the relative error on $C_n^2$ is about 28 per cent. Therefore, the relative error on the sonic seeing $\epsilon_s$ is

$$\frac{\sigma_{\epsilon s}}{\epsilon_s} = \frac{3}{5}\frac{\sigma_S}{S} = 0.17\frac{\left[\sum C_{ni}^4 \Delta z_i^2\right]^{1/2}}{\sum C_{ni}^2 \Delta z_i}. \quad (12)$$

This expression depends on the geometry of the $C_n^2$ profile. It would equal $0.17/\sqrt{5} \simeq 8$ per cent for a flat profile, and is of the same order of magnitude for the actual measured profile.

### 4.5 Bias due to spatial filtering

As it will be seen later in Section 5, sonic estimations for $C_n^2$ seem to be smaller than radiosounding ones at the lowest altitudes ($h = 8$ m, $h = 17$ m, $h = 23$ m). Indeed, sonic anemometers are known to introduce different bias effects (Travouillon et al. 2015), in particular a spatial average over the sonic impulse path. The measurement of temperature with a sonic is made between the pair of ultrasonic transducers along the vertical direction $z$. The distance between these transducers is 15 cm: small spatial fluctuations of the temperature field in the $z$ direction are smoothed over twice this distance i.e. $l' = 30$ cm because the impulse make a round trip between the sensors. An additional filtering occurs in the horizontal direction: as the integration time is not zero ($\delta t = 0.1$), sonic impulses cross a slice of atmosphere of length $v\delta t$ in the wind direction (mainly horizontal, the vertical component is weak). The effect of these two spatial filterings on the constant $C_T^2$ can be derived by writing the structure functions $D_T^2(\rho)$ as

$$D_T^2(\rho) = 2\,(\sigma_T^2 - \Gamma_T(\rho)) \quad (13)$$

where $\sigma_T^2$ is the variance of temperature fluctuations, and $\Gamma_T(\rho)$ the cross-correlation between temperatures measured at times $t$ and $t + \Delta t$ (as discussed in Section 4.1). Both quantities can be written as 3D Fourier integral over the spatial frequencies $(f_x, f_y, f_z)$. In the case of the variance we have

$$\sigma_T^2 = \iiint_{-\infty}^{\infty} W(f_x, f_y, f_z)\,\mathrm{d}^3 f, \quad (14)$$

$W(f_x, f_y, f_z)$, the 3D power spectrum of the temperature, is proportional to $|f|^{-\frac{11}{3}}$ in the range $1/L_0 < |f| < 1/l_0$ (Tatarskii 1971), $l_0$ and $L_0$ being the inner and outer scales of turbulence. Neglecting very low frequencies and assuming $l_0 = 0$ we have

$$\sigma_T^2 \propto \iiint_{\frac{1}{L_0}}^{\infty} |f|^{-\frac{11}{3}}\,\mathrm{d}^3 f. \quad (15)$$

The vertical spatial filtering of $\sigma_T^2$ is expressed by introducing the cutoff frequency $\frac{1}{l'}$ on the integral on $f_z$. Similarly, a cutoff frequency $\frac{1}{v\delta t}$ is introduced in one of the two horizontal variables (we chose $y$, but $x$ would give the same result).

$$\sigma_T'^2 \propto \int_{\frac{1}{L_0}}^{\infty}\int_{\frac{1}{L_0}}^{\frac{1}{v\delta t}} df_x\,\mathrm{d}f_y \int_{\frac{1}{L_0}}^{\frac{1}{l'}} |f|^{-\frac{11}{3}}\,\mathrm{d}f_z \quad (16)$$

so the measured variance $\sigma_T'^2$ would be lower than the expected one $\sigma_T^2$. The ratio $\sigma_T'^2/\sigma_T^2$ depends on $L_0$ and $v$; the integration of equation (16) gives 0.8 for $L_0 = 15$ m and $v = 6$ m s$^{-1}$. This bias on the variance propagates on the structure function $D_T^2(\rho)$ and therefore on the constants $C_T^2$ and $C_n^2$, which are then underestimated. We define as 'bias' the ratio of measured to expected value of $C_T^2$.

We could compensate the individual measurements from this bias, using the instantaneous wind speed provided by the sonics, and the linear model for $L_0$ described in Section 4.2. Median values found for the biases are reported in Table 2 (the error bar on these median bias was found of about 10 per cent). It appears that the lowest sonics are significantly affected (underestimation by a factor of 35 per cent for the 8 m sonic).

### 4.6 Comparison of the sonic $C_T^2$ data with microthermal measurements

In order to check the reliability of $C_T^2$ values estimated by the sonics, we made a series of simultaneous measurements with a set of two microthermal pairs (Azouit & Vernin 2005) fixed to a balsa staff near the sonic anemometer. This calibration was made at Nice Observatory in 2012 August: we just had a sonic anemometer repaired after some seasons in Antarctica, and could make the measurements before shipping it back to Dome C. The two instruments ran simultaneously for a period of $\simeq$36 h. Times series of the temperature structure function $C_T^2$ are presented in Fig. 7 . These data were not compensated from spatial filtering as presented in previous section, we indeed expect the multiplicative bias to be around 0.8, given the wind speed and outer scale at the time of the observations. The 12 h gap in the data is due to a problem with the acquisition PC. The two curves are in good agreement. In particular, they show a peak in mid-afternoon due to strong local turbulence caused by the heating of the building by the Sun. There remains a factor of 2.3 of

**Table 2.** Estimation of the multiplicative bias on the constant $C_T^2$ measured by the 6 sonics. The uncertainty is around 10 per cent.

| Sonic height (m) | 8 | 17 | 23 | 31 | 39 | 45 |
|---|---|---|---|---|---|---|
| $L_0$(m) | 7 | 11 | 12 | 16 | 19 | 21 |
| Bias on $C_T^2$ (ratio measured/expected) | 0.65 | 0.69 | 0.75 | 0.77 | 0.81 | 0.81 |

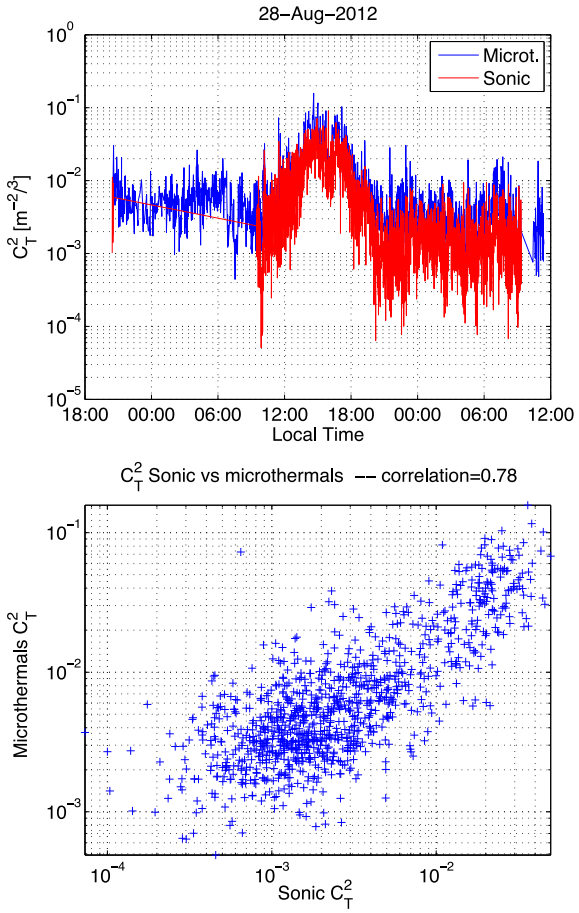


**Figure 7.** Simultaneous measurements of $C_T^2$ at Nice observatory in 2012 August. Left: times series. Right: plot of sonic $C_T^2$ versus microthermal $C_T^2$ within coincidence intervals of 30 s.

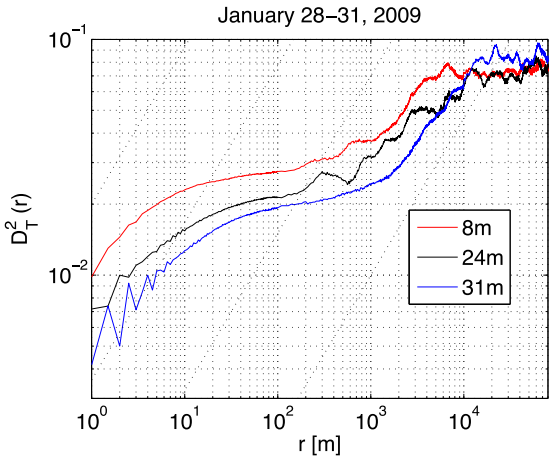


**Figure 8.** Large-scale structure function calculated on 4 d of data from 2009 Jan. 28 to Jan. 31. Oblique dashed lines have a slope 2/3.

difference in the values which would not be totally explained by the spatial filtering bias. We suspect a bad calibration of the microthermals. Fig. 7 displays also a plot of sonic $C_T^2$ versus microthermal $C_T^2$, considering coincidence intervals of 30 s between the two instruments. The correlation coefficient is 0.78. It was unfortunately not possible to perform such a calibration at Dome C during Antarctica winter conditions.

## 5 RESULTS

### 5.1 Large-scale structure functions

Coulman & Vernin (1991) reported observations of large-scale correlation between phase fluctuations of the light propagating through the turbulent atmosphere, and therefore large-scale correlation between thermodynamic parameters such as temperature or humidity. In their paper they reviewed different kind of such observations, and proposed an explanation based on the fact that at large scales (several km) the atmosphere is no longer isotropic and the troposphere may be considered as a 'thin layer' in which a 2D turbulence structure develops. The consequence for the structure function of the temperature $D_T(\rho)$ is that it behaves as $\rho^{2/3}$ for $\rho < L_0$ (inertial zone), then a saturation regime is observed for $L_0 < \rho < L_S$ with $L_S \simeq 1$ km. Then once again an inertial zone where $D_T(\rho) \propto \rho^{2/3}$ is observed for $L_S < \rho < L_M$ with $L_M$ 20 km. Saturation occurs for $\rho > L_M$.

Typical wind speeds at Dome C are a few m s$^{-1}$ near the ground, and the distance travelled by the air in one hour is about 10 km. It is then theoretically possible, with a sonic anemometer observing during one entire day, to probe structure functions $D_T(\rho)$ up to $\rho \simeq 200$ km, and even more if we take continuous data over several days. Fig. 8 shows an example of large-scale temperature structure function computed over 4 days of data, from 2009 January 28 to January 31. Data for three sonics are displayed. The three curves show exactly the behaviour predicted by Coulman & Vernin (1991): a second inertial zone starting at $L_S = 987$ m for the sonic at $h = 8$ m, $L_S = 727$ m for $h = 24$ m and $L_S = 1489$ m for $h = 31$ m. Statistical significance becomes poor at large $\rho$ and this is the reason why we considered a 4-days long data sample.

From the whole set of sonic data, we could compute, for each sonic, 378 large structure functions spanning over 4 days. Fig. 9 displays the variation of scales $L_S$ and $L_M$ as a function of the altitude, and show no significative dependence, as one could expect regarding the large numbers involved. Similarly, we found no seasonal dependence of the scales. Global statistics for $L_S$ and $L_M$ are given in Table 3.

### 5.2 Statistics of $C_n^2$

A total amount of 634000 values of valid estimations were obtained from the six sonic anemometers. Table 4 presents the statistics of the structure constant $C_n^2$ obtained at every height (the median value, and the 50 per cent confidence interval between the 25 per cent and

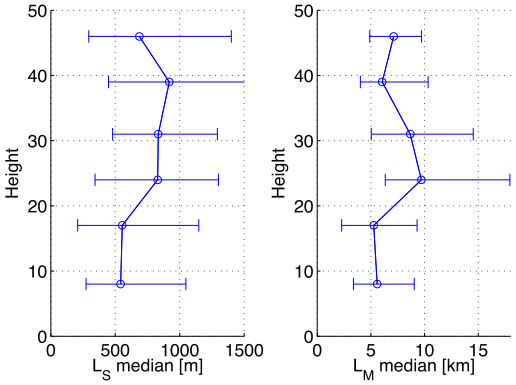


**Figure 9.** Vertical profiles of $L_S$ and $L_M$ computed from 4-days structure functions for each sonic. Error bars represent the 50 per cent confidence interval.

**Table 3.** Statistics of the scales $L_S$ and $L_M$ (boundaries of the second inertial zone) computed from 378 outer scales spanning over 4 days data sets.

| | Median | First quartile | Third quartile |
|---|---|---|---|
| $L_S$ | 713.5 m | 317 m | 1282 m |
| $L_M$ | 6.5 km | 4 km | 11 km |

the 75 per cent percentiles). At Dome C the conditions of turbulence vary strongly with the season (Aristidi et al. 2009) and we split the data into four samples corresponding to four seasons. We call here summer period when the Sun is almost circumpolar (November–January), winter when it never rises (May–July), autumn and spring being the 3-month interseasons. Statistics for both seasons are also given in Table 4. About 50 per cent of the data were collected in summer, 27 per cent in autumn, 12 per cent in spring and 11 per cent in winter.

Our values of $C_n^2$ confirm that the optical turbulence near the surface is the strongest in winter; $C_n^2$ is five to 10 times higher than in summer. Dependence of $C_n^2$ on the month is shown in Fig. 10, which displays a sinusoid-like arch with a maximum in June–July for all the sonics. These are the same sinusoidal plots that were observed for the Differential Image Motion Monitor (DIMM) seeing times series (see fig. 1 of Aristidi et al. 2009).

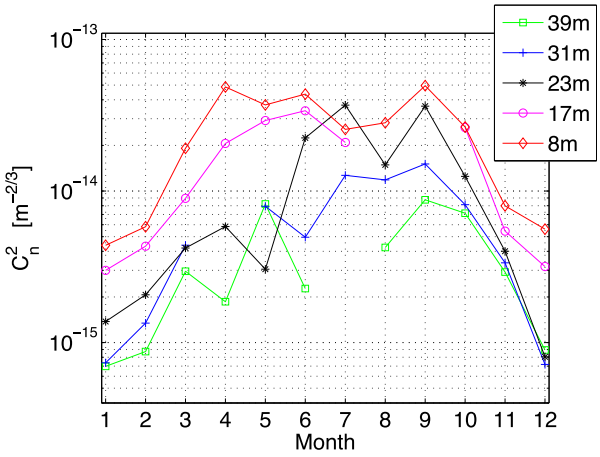


**Figure 10.** Monthly median values of the structure constant $C_n^2$ for different heights.

We compared our results with the values obtained by in situ microthermal radiosoundings performed in 2005 during the first winter-over (Trinquet et al. 2008). For this purpose we selected data from the period April–October corresponding to the months where 34 balloons were launched. Fig. 11 shows the median $C_n^2$ profile from the sonic anemometers; the superimposed dashed line is the median values measured by the radiosoundings. We also plotted the data compensated from the bias due to spatial filtering. The sonic point at $h = 45$ m is not significative (too few data). The profiles are comparable, balloon data fit with sonic error bars, though it seems that sonic points are still underestimated, even after compensation for the bias. Both curves show a rapid decay of $C_n^2$ between 8 and 45 m. However, the balloon profile presents a steeper slope: between 8 and 40 m the $C_n^2$ is divided by about 50 for the balloon data, and by 15 for the sonic data (20 if we take the bias-compensated values for sonic $C_n^2$).

Another interesting result is shown in Fig. 12. It displays the six histograms of $C_n^2$ measurements at each elevation for the period April to September, from 2008 to 2011. They show a bimodal distribution centred at values $C_n^2 = 2 \times 10^{-16}$ m$^{-2/3}$ and $C_n^2 = 2 \times 10^{-14}$ m$^{-2/3}$. The two bumps are very clear for upper heights (23 to 45 m) but the left one (centred at $C_n^2 = 2 \times 10^{-16}$ m$^{-2/3}$) exists

**Table 4.** Statistics of the structure constant $C_n^2$ at different heights above the ground. Median value and percentiles 25 per cent and 75 per cent are given. The definition of the four seasons (summer, autumn, winter and spring) is given in the text. The symbol (*) indicates a low number of data for this height and this period.

| Height (m) | $C_n^2$ (total) [$10^{-15}$ m$^{-2/3}$] | $C_n^2$ (summer) [$10^{-15}$ m$^{-2/3}$] | $C_n^2$ (autumn) [$10^{-15}$ m$^{-2/3}$] | $C_n^2$ (winter) [$10^{-15}$ m$^{-2/3}$] | $C_n^2$ (spring) [$10^{-15}$ m$^{-2/3}$] |
|---|---|---|---|---|---|
| 8 | 8.7 [3 27] | 5.1 [2 14] | 9.4 [3 29] | 36.4 [19 66] | 30.2 [11 64] |
| 17 | 6.2 [2 20] | 3.4 [1 10] | 6.8 [2 21] | 27.9 [12 56] | 29.3 [6 128] (*) |
| 24 | 2.5 [0.5 10] | 1.5 [0.4 6] | 2.8 [0.5 10] | 3.1 [0.4 8] (*) | 16.1 [4 39] |
| 31 | 2.2 [0.4 11] | 1 [0.3 4] | 2.8 [0.45 13] | 9.7 [1.2 25] | 9.8 [1 29] |
| 39 | 1.6 [0.3 9] | 1 [0.3 4] | 1.5 [0.2 8] | 2 [0.3 14] | 6.6 [0.6 25] |
| 45 | 0.9 [0.2 6] | 0.7 [0.2 4] | 1 [0.2 8] | (⋆) | 3.4 [0.2 22] |

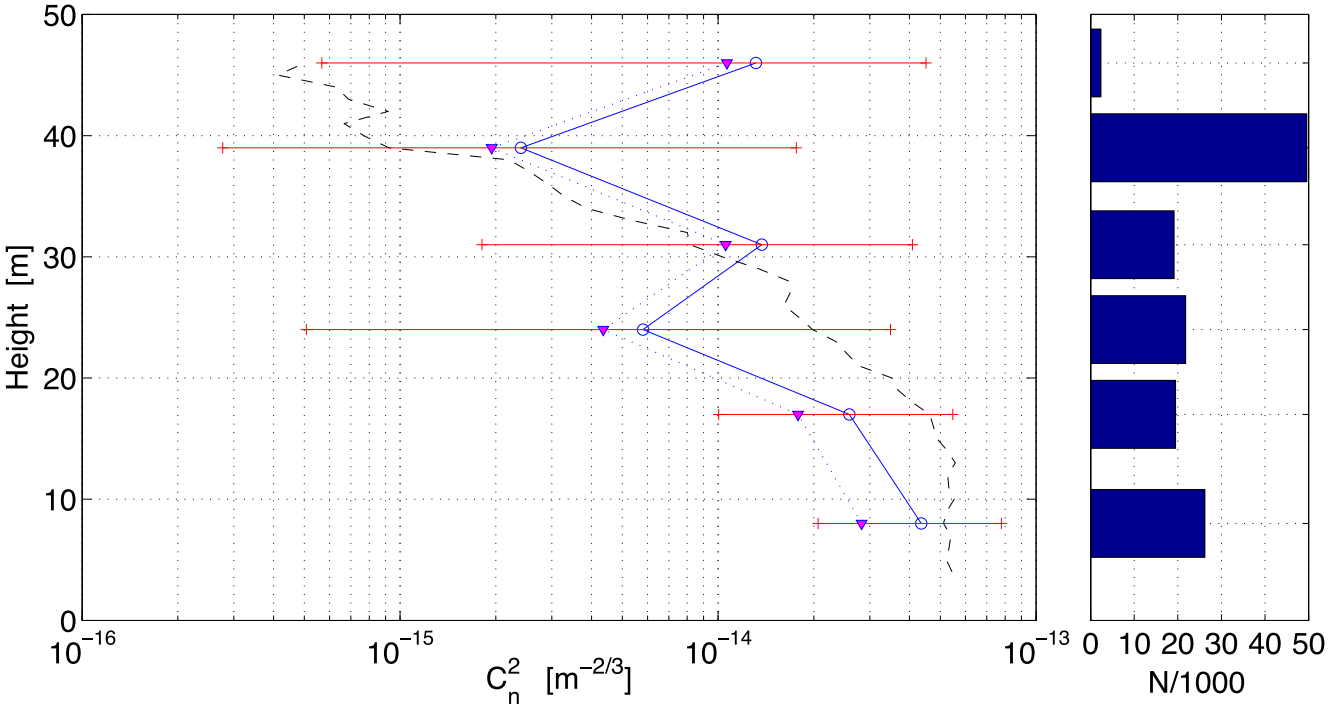


**Figure 11.** $C_n^2$ median profile for the period April–October. Blue circles: values corrected from the bias as described in Section 4.5. Triangles: raw values. Error bars are the 50 per cent confidence interval around the blue circles. The dashed line is the median profile obtained in 2005 (March 15 to October 19) from in situ radiosoundings. The histogram on the right is the number $N$ of valid sonic data at each altitude.

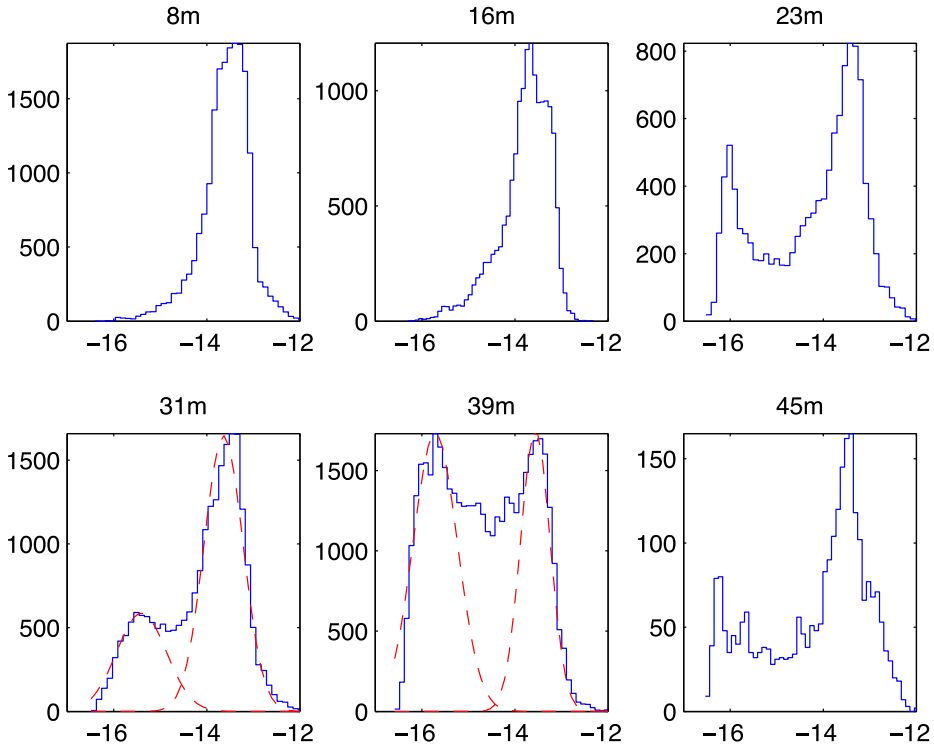


**Figure 12.** Histograms of log $C_n^2$ at different heights for the period April–September. Data corresponding to heights 31 and 39 m were fitted by a sum of two Gaussian (dashed red curves).

also at $h = 16$ m (with very small amplitude). These distributions are similar to DIMM histograms described in Aristidi et al. (2009) and the interpretation is similar: the bump on the right (resp. left) corresponds to situations where the sonic is above (resp. inside) the SL. There exist also a few intermediate situations corresponding to the cases where either the SL is not unique, but contains a second layer above, or the SL upper limit is just in front of the sonic and moves slightly up and down during the 1 min time interval other

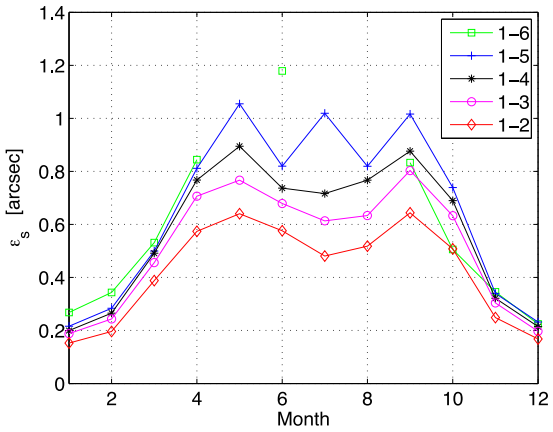


**Figure 13.** Monthly median values of the SL seeing $\epsilon_s$ integrated between 8 m and the altitude of each sonic. Label such as '1–3' means an integration between the first sonic ($h = 8$ m) and the third ($h = 24$ m).

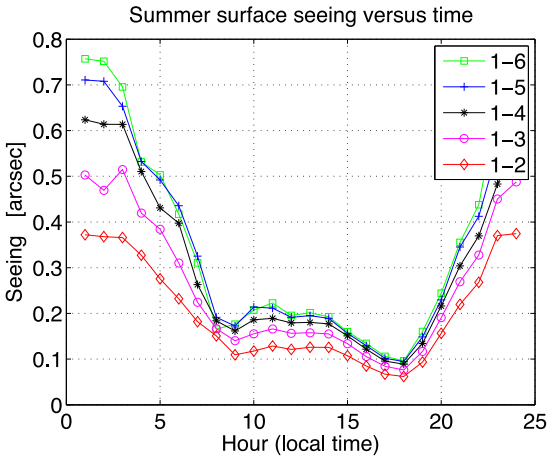


**Figure 14.** Hourly median values of the SL seeing $\epsilon_s$ in summer (the period considered here is 2008 December where all six sonics were in operation), integrated between 8 m and the altitude of each sonic. Label such as '1–3' means an integration between the first sonic ($h = 8$ m) and the third ($h = 24$ m).

which the constant $C_n^2$ is estimated. These situations correspond to 14 per cent of the measurements at $h = 31$ m and 22 per cent at $h = 39$ m.

From these histograms, it can be seen that the sonic at $h$ =31 m spends more time inside the SL (the right bump is higher than the left one). The situations are more equilibrated at $h = 39$ m. On these two particular histograms, we performed a least-squares fit of the sum of two Gaussians (indeed lognormal functions since the horizontal axis is in log scale). The fits are drawn in dashed red on the curves. The ratio of the surface of the two Gaussians (left/right) is $r_{31} = 0.44$ at $h$ =31 m and $r_{39} = 1.45$ at $h = 39$ m. A mere interpolation would give a ratio $r_h = 1$ at $h = 35$ m, which is an estimation of the thickness of the SL. It is compatible with previous measurements as well as turbulence modelling (see Aristidi 2012 and references therein).

### 5.3 Seeing statistics

Using equation (10) we could calculate the seeing $\epsilon_s$ in the SL, between the first sonic at $h = 8$ m and all the other sonics, up to $h = 45$ m. The data sample used for computing the seeing represents about 20 per cent of the number used for $C_n^2$ statistics. The reason is that we rejected the situations where the lower sonic either did not work or was the only sonic to work. Fig. 13 shows the monthly evolution of the median of $\epsilon_s$. Error bars (50 per cent confidence intervals) are $\pm 0.1$ arcsec in summer and $\pm 0.4$ arcsec in winter. The curves have a sinusoidal shape very similar to the DIMM curves displayed in fig. 1 of Aristidi et al. (2009).

Looking at the height 39 m, it can be seen that during the April–October period the median seeing inside the SL (between 8 and 39 m) is around 1 arcsec, which is consistent with the value of 1.2 arcsec derived from the 2005 radiosoundings (Trinquet et al. 2008).

### 5.4 The peculiar summer situation

Turbulence monitoring at Dome C began in 2003 with the first summer site-testing campaigns. It was noticed (Aristidi et al. 2005) that the seeing was very low with a deep minimum every day near 5 pm local time. Indeed, meteo radiosoundings have shown that the vertical temperature profile is flat twice a day: in the morning around at 10 am local time, and in the middle of the afternoon (see fig. 10 of Aristidi et al. 2005). The installation of the sonics in 2007 allowed monitoring of the SL seeing $\epsilon_s$ in summer, and particularly its dependence with time. The result, computed from 2008 December sonic data, is shown in Fig. 14 and is very interesting. We found that $\epsilon_s$ also shows, as expected, a deep minimum near 5 pm local time. At this minimum, the curves labelled '1–4', '1–5' and '1–6' are coincident: it means that the quasi-totality of the SL turbulence is below the fourth sonic (height 31 m). But there is also another minimum, though a little less deep, at 9 am. It corresponds to the temperature gradient inversion observed in the morning. Moreover, this secondary minimum was not present on the seeing curve provided by the DIMM during the 'night' hours, i.e. from 11 pm to 2 am (there is no night in summer, but a period when the Sun is low on the horizon), the SL seeing is rather strong, and spread over the whole height of the tower. The value of $\epsilon_s$ between 8 and 45 m at 0 am is $\epsilon_s \simeq 0.75$ arcsec and the total seeing $\epsilon_d$ observed by the DIMM at the same time is $\epsilon_d \simeq 0.9$ arcsec; the difference $[\epsilon_d^{5/3} - \epsilon_s^{5/3}]^{3/5}$ gives 0.4 arcsec, which is almost exactly the free atmosphere seeing as mentioned by Aristidi et al. (2009).

### 5.5 Coherence time

Statistics of the sonic coherence time $\tau_s$ (i.e. contribution of the SL) were computed on a sample containing about 300 000 valid data. A strong dependence with the season was found as expected. Fig. 15 displays the evolution of the monthly median values of $\tau_s$ for each layer. Unsurprisingly, the turbulence is faster in winter, and the curves display a sinusoidal arch which is minimum in July–August with a value $\tau_s \simeq 8$ ms.

A partial comparison of our results can be made with values of Trinquet et al. (2008). In their table 2 they give the statistics of the coherence time $\tau_0$ computed at $h = 8$ m and $h = 33$ m in autumn, winter and spring. Making use of the integral expression of $\tau_0$ given in equation (5), we could estimate the contribution $\tau_s^b$ of the layer between 8 and 33 m, and compare it with our value of $\tau_s$ in the layer between the sonics 1 and 4 ($h = 31$ m). Results are displayed in Table 5, and show that the two instruments give consistent measurements.

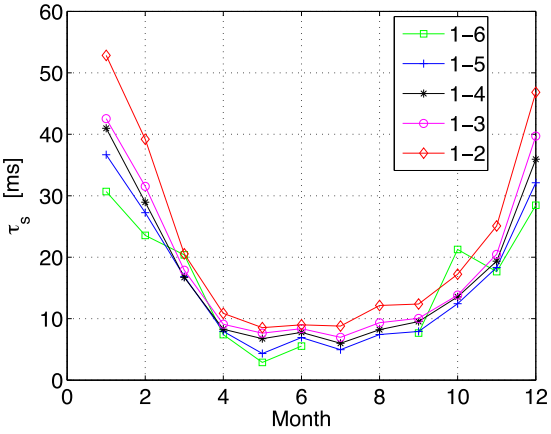


**Figure 15.** Monthly median values of the coherence time SL $\tau_s$ integrated between 8 m and the altitude of each sonic.

**Table 5.** Comparison of the SL coherence time computed from balloon data (Trinquet et al. 2008a) and sonic data. Balloon values are calculated for the layer between 8 and 33 m. Sonic values are calculated for the layer between 8 and 31 m: median value is given as well as the 50 per cent confidence interval between brackets.

| | $\tau_s^b$ (balloon) | $\tau_s$ (sonics) |
|---|---|---|
| Autumn | 18 ms | 24 ms [12–45] |
| Winter | 7 ms | 7 ms [5–12] |
| Spring | 16 ms | 12 ms [7–29] |

## 6 CONCLUSION

We have presented measurements of optical turbulence inside the SL at Dome C. These measurements represent 6 years of data collected by up to six sonic anemometers placed on a 45 m high tower. Sonic anemometers were chosen as an alternative to microthermal sensors, since these sensors are too fragile for the harsh conditions of Dome C.

Operation of sonic anemometers appeared to be easy in summer, with temperatures around −30°C and the largest amount of good quality data was collected in this period. Things become more difficult with the drop of temperatures in April. Despite the heating resistances wrapped around the arms of the sonics, we cannot totally prevent the deposit of frost and a lot of data were unusable (for the period May–August, only 10 per cent of the data were useful). It was also necessary to climb periodically (about once a week) the tower to remove the snow accumulated on the sonics. Also, a lot of technical problems were met as described in Section 3.

Despite these difficulties of operation, and thanks to the long running period, interesting results could be derived. Temperature structure functions are the basis of the work, and we found that they behave as predicted, with an inertial regime in $\rho^{2/3}$ and a saturation for larger scales of a few tens of metres. Dynamic outer scales could be measured at the intersections on these two regimes. They increase with altitude with a slope $\simeq$0.4 as predicted for isotropic turbulence. Structure functions were probed for large scales and show a second inertial zone in the range $\rho \in$ [1–10] km as predicted by Coulman & Vernin (1991). To our knowledge this is the first time that such observations are reported since the 1991 paper.

Temperature structure constants $C_T^2$ were compared to simultaneous microthermal measurements which gave satisfactory coherence (though the comparison was made in temperate temperature conditions). Some bias was observed between the sonic $C_n^2$ and the balloon-borne microthermal radiosoundings, and could be explained by spatial filtering of temperature fluctuations due to the size of the sonic arms and the finite integration time. The overall behaviour of the SL turbulence at Dome C is consistent with previous studies by different technologies: balloon-borne microthermals (Trinquet et al. 2008), DIMMs at different elevations (Aristidi et al. 2009) and SODAR (Petenko et al. 2014). They are also consistent with turbulence modelling by Lascaux et al. (2011). The sonics allowed a new estimation of the thickness of the SL in winter (35 m) which agrees here again with previous estimations.

Integrated parameters (seeing and coherence time) could be calculated in the SL. The large amount of data allowed us to make significant statistics and to probe their dependence on the season. In particular, this is the first time that these parameters are measured during the summer. We found that the SL is responsible for about 1 arcsec of the total seeing in winter. In summer, the SL seeing exhibits every day two minima with very low values, one in the afternoon and one in the morning; these two minima correspond to the inversion of the vertical temperature gradient observed by the radio-soundings.

This study shows that sonic anemometers are a viable option to undertake SL turbulence monitoring. However, attention has to be paid to data processing, especially for bias compensation and bad points removal, and it was one of the difficulties of this work. Measurements obtained here are consistent with what was previously known from various technologies and give confidence on the whole results set. One of the advantages of the sonics is the possibility to infer the properties of temperature and refractive index structure functions at small and large spatial scales, which is not so common in the panorama of available instruments. The weak point was the sensitivity to harsh climatic conditions, but it is a common problem for every instrument operating in Antarctica. This study was conducted within the polar program AstroConcordia, which terminated in 2012. This paper is one of the last from our group on the topic of Dome C site characterization for astronomical purposes.

## ACKNOWLEDGEMENTS

The authors gratefully acknowledge the polar agencies IPEV and ENEA for their logistic and financial support to our programmes (IPEV/AstroConcordia, IPEV/CALVA and INSU/CLAPA). Thanks are also due to the US NSF and the French agencies INSU and ANR for funding. We are in debt to the Dome C local staff and winterovers from 2007 to 2012 for their assistance, in particular to people who climbed the tower to remove the snow on the sonics. Thanks also to Herb Zimmerman from Applied Technologies for technical support and advice throughout these years.

## REFERENCES

Aristidi E., 2012, in Boissier S., de Laverny P., Nardetto N., Samadi R., Valls-Gabaud D., Wozniak H., eds, SF2A-2012: Proc. Annual Meeting of the French Society of Astronomy and Astrophysics, p. 697
Aristidi E. et al., 2005, A&A, 444, 651
Aristidi E. et al., 2009, A&A, 499, 955
Azouit M., Vernin J., 2005, PASP, 117, 536
Bonner C. et al., 2010, PASP, 122, 1122
Carbillet M., Maire A.-L., Le Roux B., Aristidi E., Giordano C., Pasqueron de Fommervault O., Gautier J., Trinquet H., 2010, in Spinoglio L., Epchtein N., eds, EAS Publications Series, Vol. 40, EAS Publications Series, p. 157
Coulman C. E., Vernin J., 1991, Appl. Opt., 30, 118

Fossat E., Aristidi E., Agabi A., Bondoux E., Challita Z., Jeanneaux F. D. M., 2010, A&A, 517, 955
Friehe C. A., 1976, J. Appl. Meteorol., 15, 607
Genthon C., Six D., GalléE H., Grigioni P., Pellegrini A., 2013, J. Geophys. Res. (Atmospheres), 118, 3218
Hagelin S., Masciadri E., Lascaux F., Stoesz J., 2008, MNRAS, 387, 1499
Kaimal J. C., 1979, in Kovasznay L. S. G., Favre A., Buchhave P., Fulachier L., eds, Proc. Dynamic Flow Conference, Dynamic Measurements in Unsteady Flows. Marseille, France, p. 551
Lascaux F., Masciadri E., Hagelin S., Stoesz J., 2009, MNRAS, 398, 1093
Lascaux F., Masciadri E., Hagelin S., 2010, MNRAS, 403, 1714
Lascaux F., Masciadri E., Hagelin S., 2011, MNRAS, 411, 693
Lawrence J.-S., 2004, PASP, 116, 482
Lawrence J., Ashley M., Tokovinin A., Travouillon T., 2004, Nature, 431, 278
Marks R., Vernin J., Azouit M., Manigault J.-F., Clevelin C., 1999, A&A, 134, 161
Mosser B., Aristidi E., 2007, PASP, 119, 127
Nakayama Y., Boucher R.-F., 2000, Introduction to fluid mechanics. Butterworth-Heinemann
Okita H., Ichikawa T., Aschley M.-C.-B., Takato N., Motoyama H., 2013, A&A, 554, L5
Petenko I. et al., 2014, A&A, 548, 44
Roddier F., 1981, Progress Opt., 19, 281
Swain M.-R., Gallée H., 2006, PASP, 118, 1190
Tatarskii V. I., 1971, The Effects of the Turbulent Atmosphere on Wave propagation. Israel Program for Scientific Translations, Jerusalem
Travouillon T., Aristidi E., Fossat E., Lawrence J., Mékarnia D., Moore A., Skidmore A., Storey J., 2008, in Stepp L., Gilmozzi R., eds, Proc. SPIE, Vol. 7012, Ground-based and Airborne Telescopes II, SPIE, p. 70124B
Travouillon T., Jolissaint L., Ashley M., Lawrence J., Storey J.-W.-V., 2009, PASP, 121, 668
Travouillon T. et al., 2010, in Spinoglio L., Epchtein N., eds, EAS Publications Series, Vol. 40, Proc. 3rd ARENA Conference: An Astronomical Observatory at CONCORDIA (Dome C, Antarctica), Frascati, Italy, EAS Publications Series, p. 115
Travouillon T., Otarola A., Els S., Riddle R., Schöck M., Skidmore W., Bibb D., 2015, J. Phys. Conf. Ser., 595, 012036
Trinquet H., Agabi A., Vernin J., Azouit M., Aristidi E., Fossat E., 2008, PASP, 120, 203

This paper has been typeset from a TEX/LATEX file prepared by the author.